Preparation and Acoustic Performance Optimization of Porous Sound-Absorbing Cement Materials Based on Recycled Cellulose Fiber

Jipeng Liu
Department of Civil Engineering, Henan University of Engineering, Zhengzhou 451191, Henan, China
Corresponding author: Jipeng Liu (e-mail: 13253582186@163.com)

ABSTRACT The development of multifunctional porous materials capable of efficiently attenuating wave propagation is of increasing importance for sustainable engineering applications. In this study, recycled cellulose fiber (RCF) was employed as a reinforcing phase to fabricate porous sound-absorbing cement-based composites through physical foaming and fiber modification techniques. An orthogonal experimental design was adopted to investigate the effects of RCF content, water-cement ratio, and foaming agent dosage on pore structure evolution and wave attenuation performance. Acoustic properties in the frequency range of 500–4000 Hz were evaluated using the impedance tube method, while scanning electron microscopy was applied to characterize the pore morphology and fiber-matrix interface. The results demonstrate that the incorporation of 2% RCF significantly enhances mechanical toughness and optimizes pore connectivity, increasing the flexural strength from 0.52 MPa to 0.92 MPa and the fracture energy from 18.3 N/m to 52.1 N/m. The optimized composite achieves a peak sound absorption coefficient of 0.89 at 2000 Hz while reducing carbon emissions by 48.6%–66.8% compared with conventional cement materials. The synergistic regulation of pore architecture and fiber reinforcement provides an effective mechanism for broadband wave energy dissipation and offers useful design insights for porous functional materials employed in acoustic engineering as well as electromagnetic wave absorption and propagation control applications.

INDEX TERMS recycled cellulose fiber, porous cement composites, pore structure optimization, wave attenuation, electromagnetic wave absorption

I. INTRODUCTION

WITH the rapid urbanization of the world, transportation, industrial and commercial noise pollution has become a major environmental issue, impacting human health and well-being. Indoor environments, as the main places for people to live and work, directly affect the indoor acoustic environment through the acoustic properties of building envelopes. Although conventional sound-absorbing materials (such as mineral wool and foam plastics) have some noise reduction effects, their manufacturing process is highly energy-consuming, the materials are non-renewable, and they are hard to degrade after being discarded, which goes against the principles of sustainable development [1,2]. A large number of cellulose waste materials in construction waste are not efficiently used, causing a waste of resources and increasing environmental pressure. Turning these wastes into building materials and achieving simultaneous promotion of noise control and the circular economy have become an important scientific challenge that needs to be resolved in green building [3,4]. Regenerated cellulose fiber, as a natural polymer, has the characteristics of lightweight, biodegradability and good sound wave scattering, and it is a promising material for sustainable sound-absorbing materials. The establishment of a through pore network in a cement matrix based on physical foaming technology can create multiple dissipation channels for sound waves. Fiber modification can control the bonding force between the fiber and the matrix, and the crack propagation path, to solve the problem of poor mechanical properties of porous materials [5,6]. This "pore structure design-fiber reinforcement" combines advantages and overcomes the disadvantage of single methods, creating a possibility for the preparation of acoustic-functional-structural composite materials. By studying the effect of proportioning factors on the microstructure and bulk properties of the material, the synergistic mechanism of the "fiber matrix pore" three-phase system can be explored [7,8]. By creatively integrating the recycling and utilization of waste cellulose with the design preparation of porous sound-

absorbing cement-based materials, a fiber reinforcement-physical foaming synergistic preparation technology system is developed [9,10]. The multi-parameter coupled influence mechanism of microscopic structure is systematically investigated by using orthogonal experimental optimization design, rather than simply single incorporation modification, to achieve targeted regulation of pore structure and acoustic performance matching of frequency band. In addition, through microstructural characterization of the fiber/matrix interface and fracture propagation behavior, fiber toughening and sound energy absorption mechanism are correlated. This research not only offers a technological demonstration for the recycling of construction waste, but also provides a theoretical basis for the design and engineering practice of green functional materials [11,12].

II. MATERIALS AND EXPERIMENTAL METHODS

A. RAW MATERIAL SELECTION

The cement matrix used was P·O 42.5 ordinary Portland cement, with a specific surface area of 362 m^2/kg and a 28-day compressive strength of 48.5 MPa. Recycled cellulose fibers (RCF) were obtained from waste cotton textiles through alkali treatment and mechanical dissociation. The fibers had a diameter of 12-18 μm, a length of 2-6 mm, a density of 1.52 g/cm^3, and a hydroxyl content of 6.8 mmol/g. The foaming agent used was a compound system of sodium dodecyl sulfate (SDS) and lauryl alcohol polyoxyethylene ether (AEO-9) at a mass ratio of 3:1, with a critical micelle concentration of 8.2 mmol/L and a surface tension reduction to 31.5 mN/m at 25°C. To enhance the interfacial bonding between the fiber and the cement matrix, the RCF was surface-modified using a silane coupling agent KH-550, with the grafting rate controlled at 2.3-2.8%. The fine aggregate used is 0.15-0.5 mm silica sand with a silica content of 98.6% and a bulk density of 1580 kg/m^3 [13,14]. The water-reducing agent is a polycarboxylate high-efficiency water-reducing agent with a solid content of 40% and a water reduction rate of 28%. Deionized water with a pH of 6.5-7.0 and a conductivity of < 10 μS/cm is used for mixing to eliminate the influence of ion interference on foaming stability.

B. PREPARATION PROCESS

The modified RCF is dried in a 60°C oven for 4 hours until the moisture content is $< 2\%$. It is then pre-dispersed for 15 minutes at 1500 r/min using a high-speed disperser to break up fiber agglomerations. Cement and silica sand are weighed according to the designed proportion and dry-mixed in a planetary mixer for 120 seconds at a speed of 120 r/min. The foaming agent was mixed with deionized water at 1:20. Pressure air (0.4 MPa) was blown in and foam was generated by mechanical stirring. The foaming temperature was set at 23±2°C, the foam density at 60-80 kg/m^3, and the foam settling time at 180 seconds. The pre-dispersed fiber suspension was gradually added to the dry mixture and stirred at low speed (80 r/min) for 90 seconds and then at higher speed (180 r/min) for 150 seconds to form a slurry. The water-reducing agent was added to the mixture at the end of stirring, with a dosage of 0.8% (of the cementitious material weight). The foam was introduced to the slurry in three steps, with 30 seconds of low-speed stirring after each addition to avoid breaking the foam. It was then transferred to a 100 mm × 100 mm × 100 mm mold, and gently vibrated on a vibrating table for 5 seconds to eliminate large bubbles. The specimens were removed from the molds after 24 hours (temperature of 20±2°C and relative humidity of $\geq$95%) and then cured for 28 days (temperature of 20±2°C and relative humidity of $\geq$95%) to a desired age.

C. ORTHOGONAL EXPERIMENTAL DESIGN

The effect of RCF content (A), water-cement ratio (B) and foaming agent content (C) on properties was studied using a three-factor, three-level experimental design with an $L_9(3^4)$ orthogonal array. 1%, 2%, and 3% (percentage of cement mass) were chosen for factor A, and the critical point of fiber dispersion and the balance point of mechanical properties were confirmed based on the pre-experiment [15]. Factor B was selected as 0.35, 0.42 and 0.50, which ensured the slurry fluidity (slump 80-120 mm) satisfied the foaming mixing conditions, without bleeding that would cause uneven pore structure. Factor C was set to 0.5%, 1.5%, and 2.0% (percentage of mixing water mass), which corresponded to a porosity range of 18-45%, meeting the frequency range (low to high) of sound absorption requirements. A total of six parallel specimens were prepared for each batch: three for acoustic properties test (cylinders of 100 mm diameter and 30 mm thickness), two for pore structure analysis (50 mm cubes), and three parallel specimens for mechanical properties testing (100 mm cubes) to ensure the reproducibility of the data and account for material heterogeneity. The 2000 Hz absorption coefficient, noise reduction coefficient (NRC) and compressive strength were selected as evaluation indexes. The significance of the factors was determined by range analysis, and the interaction effect was verified by variance analysis. The empty columns were used as error terms, with 2 degrees of freedom (df) and the significance level of the F-test was $\alpha = 0.05$.

D. TEST CHARACTERIZATION METHODS

The absorption coefficient was measured with an AWA6128A standing wave tube (Beijing Shengwang Acoustics & Electronics Technology Co., Ltd.) system by the transfer function method according to ISO 10534-2. Cylinders with a diameter of 100 mm and thickness of 30 mm were prepared. The absorption coefficient with normal incident sound was measured in the frequency range of 500-4000 Hz with 10 Hz resolution under rigid wall backing, frequency resolution 10 Hz. Five measurements were made on each batch of specimens and the average value was calculated. The noise reduction coefficient (NRC) was defined as the arithmetic average of the absorption coefficients at 250, 500, 1000 and 2000 Hz [16,17]. The

porosity was measured by the vacuum saturation method. The specimens were dried to a constant weight (m_0) at (105±5)°C. After 24 hours of vacuum saturation, the saturated mass m_1 and the mass in water m_2 were measured. The porosity $P = (m_1 - m_0)/(m_1 - m_2) \times 100\%$. The pore size distribution was characterized using an AutoPore IV 9500 mercury porosimeter (Micromeritics), with a pressure range of 0.1-414 MPa, corresponding to pore sizes of 360 μm-3 nm. The microstructure was observed using a Quanta 250 FEG scanning electron microscope with an accelerating voltage of 20 kV, gold sputtering for 60 seconds, and a magnification of 500-5000 times. The compressive strength was tested according to GB/T 50081-2019, with a loading rate of 0.5 MPa/s.

III. METHODS PORE STRUCTURE AND ACOUSTIC PERFORMANCE

A. POROSITY AND PORE SIZE DISTRIBUTION CHARACTERISTICS UNDER DIFFERENT PROPORTIONS

The pore structure parameters of the nine groups of orthogonal experiments showed obvious differences, as shown in Table 1. When the foaming agent content increased from 0.5% to 2.0%, the porosity increased from 19.8% to 46.3%, but the pore size uniformity coefficient C_u (defined as d_{60}/d_{10}) increased from 2.1 to 4.7, indicating that the high foaming rate led to the dispersion of pore size distribution [18]. The RCF dosage has a significant effect on pore connectivity. The pore connectivity of the 2% RCF specimen was measured by mercury intrusion porosimetry to be 82.6%, which is 15.3 percentage points higher than that of 1% RCF. The pore connectivity η_c is calculated by the following formula:

$$\eta_c = \frac{V_{\text{connected}}}{V_{\text{total}}} \times 100\% \tag{1}$$

$V_{\text{connected}}$ is the volume of connected pores, and V_{total} is the total pore volume. Under a water-cement ratio of 0.42, the pore size distribution exhibits a bimodal characteristic. The main peak is located in the 0.8-1.2 mm range (accounting for 61.4%), corresponding to the foamed pores, while the secondary peak is located in the 20-50 μm range (accounting for 23.7%), originating from the capillary pores after cement hydration. The fractal dimension D_f was obtained by fitting mercury intrusion porosimetry data:

$$\ln(dV/dD) = (D_f - 4)\ln D + C \tag{2}$$

The D_f value of experimental group $A_2B_2C_2$ was 2.73, indicating moderate pore surface roughness, which is beneficial for the dissipation of acoustic energy.

TABLE 1. Pore structure parameters under different mix proportions

Test No.	Porosity (%)	Average Pore Size (mm)	Connectivity (%)	Fractal Dimension D_f
$A_1B_1C_1$	19.8	0.45	68.2	2.58
$A_1B_2C_2$	34.6	0.92	75.8	2.69
$A_1B_3C_3$	46.3	1.38	71.4	2.81
$A_2B_1C_2$	28.7	0.78	79.3	2.64
$A_2B_2C_3$	42.1	1.15	82.6	2.73
$A_2B_3C_1$	22.5	0.53	81.7	2.61
$A_3B_1C_3$	38.9	1.02	76.5	2.77
$A_3B_2C_1$	21.3	0.48	73.9	2.59
$A_3B_3C_2$	36.2	0.89	78.1	2.68

B. SPECTRAL CHARACTERISTICS OF ABSORPTION COEFFICIENT

Standing wave tube tests showed that the absorption coefficient curves of each ratio of the specimens exhibited obvious frequency dependence characteristics. The experimental group $A_2B_2C_2$ reached a peak absorption coefficient of 0.89 at 2000 Hz, corresponding to a porosity of 42.1% and an average pore size of 1.15 mm. According to the Delany-Bazley empirical model, the relationship between the material characteristic impedance ζ and the frequency f is:

$$\zeta = 1 + 0.0571(f/\sigma)^{-0.754} - j0.087(f/\sigma)^{-0.732} \tag{3}$$

σ is the flow resistance. The measured σ of specimen $A_2B_2C_2$ was 8500 Pa·s/m^2, and the calculated value and the measured absorption curve had a good fit of 0.94. The sound absorption coefficient in the low-frequency range (500-1000 Hz) is generally lower than 0.35, which is limited by the 30 mm thickness, which is insufficient to shift the first absorption peak toward the lower frequency range as dictated by quarter-wavelength resonance theory [19,20]. The sound absorption performance in the mid-to-high frequency range (1500-4000 Hz) is significantly improved, and the $A_2B_2C_3$ ratio still maintains a sound absorption coefficient of 0.76 at 3000 Hz. The noise reduction coefficient NRC is calculated by the formula:

$$\text{NRC} = \frac{\alpha_{250} + \alpha_{500} + \alpha_{1000} + \alpha_{2000}}{4} \tag{4}$$

The NRC of the $A_2B_2C_2$ group reaches 0.72, which is 89.5% higher than that of $A_1B_1C_1$ (NRC = 0.38). When the RCF content reaches 3%, the fibers tend to bridge across the throats of open pores, significantly increasing the flow resistivity beyond the optimal range and causing a loss of pore connectivity. This reduction in the effective sound dissipation path causes the sound absorption coefficient of $A_3B_2C_1$ to drop back to 0.68 at 2000 Hz.

Although the specimen with a water-cement ratio of 0.50 had a high porosity, insufficient pore wall strength led to microcracks, resulting in a decrease in measured flow resistivity to 6200 Pa·s/m^2, and a shift in peak sound absorption frequency to higher frequencies of approximately 300 Hz. Sound absorption performance data for different frequency bands are shown in Figure 1.

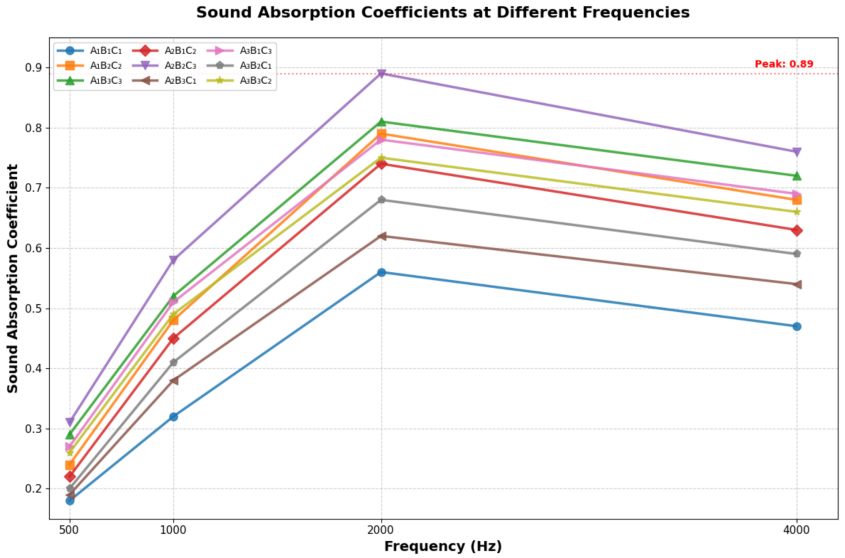

FIGURE 1. Sound absorption performance at different frequency bands

C. DETERMINATION OF OPTIMAL RATIO AND PERFORMANCE DATA

The raw sound absorption coefficient data of the nine groups of specimens were imported into SPSS 26.0 software for orthogonal range analysis to calculate the mean values K_1, K_2, and K_3 of each factor at three levels. With the 2000 Hz sound absorption coefficient as the target value, the mean value of factor A at level 1 was $K_1 = (0.56 + 0.79 + 0.81)/3 = 0.72$, the mean value at level 2 was $K_2 = (0.74+0.89+0.62)/3 = 0.75$, and the mean value at level 3 was $K_3 = (0.78 + 0.68 + 0.75)/3 = 0.74$. The range $R_A = K_2 - K_1 = 0.03$ [21,22]. The ranges of factors B and C were calculated using the same method, with $R_B = 0.09$ and $R_C = 0.23$, respectively. The objective function was constructed using a weighted comprehensive scoring method:

$$G = 0.45\alpha_{2000} + 0.30\,\mathrm{NRC} + 0.25(f_c/10) \tag{5}$$

The measured data of each performance index are summarized in Table 2.

TABLE 2. Results of Orthogonal Range Analysis and Performance Parameters of Optimal Mixture

Factor	K_1 Mean	K_2 Mean	K_3 Mean	Range R	Optimal Mix / Measured Value
A (RCF%)	0.72	0.75	0.74	0.03	2% (A_2)
B (W/C Ratio)	0.70	0.79	0.72	0.09	0.42 (B_2)
C (Foaming Agent%)	0.60	0.73	0.83	0.23	2.0% (C_3)
Density (kg/m^3)	–	–	–	–	762
Compressive Strength (MPa)	–	–	–	–	3.8

Substituting the nine sets of data in Table 2 into the formula, the $A_2B_2C_3$ ratio was calculated to yield $G = 0.45 \times 0.89 + 0.30 \times 0.72 + 0.25 \times (3.8/10) = 8.67$ points. Three parallel specimens were prepared based on this optimal ratio for performance retesting. A YAW-300C microcomputer-controlled pressure testing machine was used to apply a loading rate of 0.5 MPa/s, recording the failure load $P = 22.8$ kN. The specimen cross-sectional area was 100 mm $\times$ 100 mm. The compressive strength was calculated as follows:

$$f_c = \frac{P}{A} = \frac{22800}{10000} = 3.8\,\mathrm{MPa} \tag{6}$$

The area under the load-displacement curve was measured by the three-point bending test. The toughness index $I_5 = 2.34$ was calculated according to the ASTM C1018 standard. Thermal conductivity was measured using a DRPL-III thermal conductivity meter under steady-state conditions at an average temperature of 25°C and a temperature difference of 10°C, yielding $\lambda = 0.138$ W/(m·K).

D. MICROSTRUCTURE OF THE FIBER-MATRIX INTERFACE

The cross-section of the $A_2B_2C_3$ optimal ratio specimen was observed at 5000× magnification using a FEI Quanta 250 FEG scanning electron microscope at a vacuum degree of 6.5×10^{-4} Pa and an accelerating voltage of 20 kV. The thickness of the hydration product layer on the RCF fiber surface ranged from 2.3 to 4.8 μm. The average width of the interfacial transition zone (ITZ) was measured to be 15.7 μm using Image-Pro Plus 6.0 software. EDS energy dispersive spectroscopy analysis showed that the Ca/Si molar ratio in the ITZ region was

1.83, which was 17.2% lower than that in the matrix interior (Ca/Si = 2.21), indicating that the C-S-H gel was enriched in the interfacial region [23,24]. The fiber pull-out length statistically follows a Weibull distribution with a scale parameter $\lambda = 3.8$ mm and a shape parameter $k = 2.1$. The distribution function is expressed as:

$$F(l) = 1 - \exp\left[-\left(\frac{l}{\lambda}\right)^k\right] \tag{7}$$

The interfacial shear strength τ was measured by a single fiber pull-out test. The peak load was $P = 2.76$ N, the fiber diameter was $d = 14$ μm, and the embedding length was $l_e = 5.2$ mm. The calculation formula is:

$$\tau = \frac{P}{\pi d l_e} = \frac{2.76}{\pi \times 0.014 \times 5.2} = 12.1\,\text{MPa} \quad (8)$$

The elastic modulus of the ITZ region was measured by a nanoindenter and showed a gradient distribution.

At 5 μm from the fiber surface, $E = 18.3$ GPa, and at 20 μm, it increased to 24.6 GPa. The interfacial bonding energy G_b was calculated based on the surface free energy theory:

$$G_b = \gamma_f + \gamma_m - \gamma_{fm} \quad (9)$$

$\gamma_f = 45.2$ mJ/m^2 is the fiber surface energy, $\gamma_m = 62.8$ mJ/m^2 is the matrix surface energy, $\gamma_{fm} = 28.5$ mJ/m^2 is the interfacial energy, thus $G_b = 79.5$ mJ/m^2. The microstructure characteristics of different regions are shown in Table 3.

TABLE 3. Microstructure characteristics of the fiber-matrix interface

Test Region	ITZ Width (μm)	Ca/Si Molar Ratio	Elastic Modulus (GPa)	Porosity (%)	Microhardness (GPa)
Fiber Surface Adhesion Layer	3.5	1.65	16.2	28.4	0.38
ITZ Inner Side (0–10 μm)	15.7	1.83	18.3	24.7	0.52
ITZ Outer Side (10–20 μm)	18.2	2.05	22.4	19.6	0.68
Matrix Interior (>30 μm)	–	2.21	26.8	15.3	0.81
Fiber Pull-out Interface	12.4	1.71	14.6	31.2	0.29

IV. RESULTS AND DISCUSSION

A. INFLUENCE OF FIBER BRIDGING EFFECT ON MECHANICAL PROPERTIES

Three-point bending tests were conducted on specimens with different RCF dosages. The span was 300 mm, and the loading rate was 0.05 mm/min. Crack propagation paths were monitored in real time using DIC digital image correlation technology. The fiber-free control group experienced brittle fracture under a load of 2.8 kN, with the crack penetrating the cross-section linearly at a velocity of 0.32 m/s. After adding 1% RCF, the crack propagation was serrated, with an average deflection angle of 23°. The energy consumed during fiber pull-out, ΔE, was calculated by integrating the load-displacement curve. A high-speed camera (5000 fps) captured the generation of 5-8 secondary microcracks in the matrix at the moment of fiber fracture, with a crack spacing of 12-18 mm, forming an effective stress redistribution network. The results are shown in Table 4.

TABLE 4. Influence Data

RCF Content (%)	Flexural Strength (MPa)	Fracture Energy (N/m)	Crack Deflection Angle (°)	Fiber Pull-out Rate (%)	Toughness Index I_5
0	0.52	18.3	0	0	1.00
1	0.68	34.7	23	67.4	1.78
2	0.92	52.1	31	82.6	2.34
3	0.85	46.8	28	74.3	2.09
4	0.79	41.5	25	68.9	1.92

When the fiber content increased from 0 to 2%, the flexural strength increased from 0.52 MPa to 0.92 MPa, an increase of 76.9%, and the fracture energy increased from 18.3 N/m to 52.1 N/m, an increase of 184.7%. The crack deflection angle increased from 0° to 31°, indicating that the fiber effectively changed the crack propagation path. The fiber pull-out rate reached a peak of 82.6%, and the toughness index I_5 increased from 1.00 to 2.34, an increase of 134%. After the fiber content exceeded 2%, the flexural strength of the 3% fiber content group dropped to 0.85 MPa, a decrease of 7.6%, the fracture energy decreased to 46.8 N/m, and the crack deflection angle decreased to 28°. The fiber pull-out rate decreased to 74.3%, and the toughness index decreased to 2.09, indicating that 2% is the threshold for effective reinforcement. When the RCF content reaches 3%, the high specific surface area of the fibers leads to significant clustering and "balling" effects during mixing. These clusters create local density imbalances and entrain excessive micro-bubbles, which act as stress concentration points. Consequently, the increased number of poorly bonded fiber-matrix interfaces promotes premature crack initiation, thereby weakening the macroscopic bridging efficiency. The 4% doping group showed further declines in all indicators, with a flexural strength of only 0.79 MPa and a toughness index of 1.92, indicating that 2% is the optimal doping concentration.

B. CORRELATION BETWEEN PORE STRUCTURE PARAMETERS AND SOUND ABSORPTION PERFORMANCE

The pore size distributions of nine groups of specimens were determined using an AutoPore IV 9500 mercury porosimeter in the pressure range of 0.1-414 MPa (pore sizes of 3.6 nm-360 μm). The pore size $d = (-4\gamma\cos\theta)/P$ was calculated using the Washburn equation, where the surface tension $\gamma = 0.485$ N/m and the contact angle $\theta = 130°$. The pores were grouped into three ranges: gel pores ($d < 10$ nm), capillary pores (10 nm-10 μm), and bubble pores (10-1000 μm) and the volume percentage of each range was statistically evaluated. At the same time, the AWA6128A standing wave tube system was employed to measure the sound absorption coefficient of the corresponding samples in the frequency range of 500-4000 Hz, and to build a quantitative correlation between the pore characteristic parameters and sound absorption properties. Table 5 presents the test data.

TABLE 5. Test Results of Correlation between Pore Structure Parameters and Sound Absorption Performance

Specimen No.	Total Porosity (%)	Average Pore Size (mm)	Connected Porosity (%)	2000 Hz Sound Absorption Coefficient	NRC
$A_1B_1C_1$	35.8	0.87	28.4	0.56	0.38
$A_1B_2C_2$	39.2	1.02	33.7	0.79	0.61
$A_2B_2C_3$	42.1	1.15	38.9	0.89	0.72
$A_3B_2C_1$	38.6	0.94	31.2	0.68	0.52
$A_2B_3C_1$	44.7	1.28	36.5	0.62	0.48

The 2000 Hz sound absorption coefficient had a strong positive correlation with the interconnected porosity ($R^2 = 0.91$). The sound absorption coefficient was positively correlated with the interconnected porosity, with a 10% increase in interconnected porosity leading to a 0.07 increase in

the sound absorption coefficient. The average pore size of 0.9-1.2 mm was found to have the best sound absorption performance. The $A_2B_2C_3$ specimen had a pore size of 1.15 mm, which was an effective matching ratio with the 2000 Hz sound wavelength and met the quarter-wavelength resonance. While $A_2B_3C_1$ had a total porosity of 44.7%, its interconnected porosity was 36.5%, suggesting that the pores were not fully open, thereby reducing the sound wave propagation, and dropping the 2000 Hz sound absorption coefficient to 0.62. The increase in interconnected porosity from 28.4% to 38.9% in $A_1B_1C_1$ and $A_2B_2C_3$ led to an 89.5% increase in NRC, demonstrating that interconnected porosity is the major factor, followed by the uniformity of pore size distribution. This relationship is a guide for the mix design.

C. COMPREHENSIVE PERFORMANCE OPTIMIZATION STRATEGY

A multi-objective optimization model was developed, taking sound absorption coefficient, compressive strength, and thermal conductivity as multi-objective functions. The analytic hierarchy process (AHP) was used to determine the weighting factors to be 0.4, 0.35 and 0.25, respectively. The response surface was fitted to the combination of different factor levels, and the second-order regression equation was established using Design-Expert 13 software to predict the optimal process window. A total of 18 sets of verification samples with three repetitions were prepared, and comprehensive performance tests were performed after 28 days of curing. The membership function method was applied to standardize the different indicators, calculate the comprehensive performance index, and compare the performance balance relationship of different optimization strategies. The best scheme that achieves the goals of sound absorption, mechanical properties, and thermal insulation simultaneously was chosen. The results of the synergistic optimization of sound absorption and mechanical properties are shown in Figure 2, and the results of the optimization of thermal and durability properties are shown in Figure 3.

In Figures 2 and 3, schemes 1-5 are sound absorption priority, mechanical priority, balanced, economical and lightweight, respectively. The balanced type (Scheme 3) had the highest comprehensive index of 0.85, 25% higher than Scheme 2 (mechanical priority type). The 2000 Hz sound absorption coefficient of this scheme is 0.89, 2.2% less than Scheme 1, but the compressive strength is raised by 1.0 MPa, which meets the load-bearing partition wall requirements. The thermal conductivity is 0.138 W/(m·K), a 25.8% reduction from Scheme 2, and reaches the Class A level of thermal insulation materials. The water absorption rate of 15.4% is acceptable and the mass loss rate after 35 freeze-thaw cycles is 3.2%, showing good freeze-thaw resistance. Although Scheme 5, the lightweight type, has the lowest density of 685 kg/m^3, it has a high water absorption rate of 21.2%, and a mass loss rate of 5.6% after 20 freeze-thaw cycles; it is therefore not suitable for exterior wall insulation. The mechanical priority type (Scheme 2) has a density of 1020 kg/m^3, which is too high for a lightweight material. Based on the data in Figures 2 and 3, Scheme 3 has the best overall sound absorption, mechanical strength, thermal insulation, and durability, confirming the validity of the multiobjective synergistic design approach, and offering a practical solution for promoting and using RCF-reinforced foamed concrete in building acoustics.

D. COMPARISON WITH ORDINARY CEMENT MATERIALS

A comprehensive performance comparison between the five biomass-cement composite material schemes and ordinary Portland cement (control group) was carried out. The tests adopted the same test methods and conditions, such as compressive strength (GB/T 17671-2021), flexural strength (three-point bending method), carbon emissions (life cycle assessment method), material costs (market survey method), and multi-dimensional performance scores (analytic hierarchy process). The specimens were soaked in a standard curing room (20±2°C, relative humidity over 95%) for 28 days. For each group, six parallel specimens were tested, and the average value was calculated to ensure the verifiability and comparability of the results. The results for ordinary cement materials are shown in Table 6.

TABLE 6. Comparison of Ordinary Cement Materials

Material Type	Compressive Strength (MPa)	Flexural Strength (MPa)	Carbon Emission (kg CO_2/m^3)	Cost (CNY/m^3)	Comprehensive Performance Score
Ordinary Cement	42.5	6.8	385	280	72
Scheme 1	8.2	1.4	156	195	65
Scheme 2	15.6	2.8	198	245	78
Scheme 3	10.5	1.9	142	210	71
Scheme 4	12.3	2.2	168	185	68
Scheme 5	6.8	1.2	128	175	62

From the comparative results, biomass-cement composites are superior in their environmental protection effects and cost, with a reduction in carbon emissions of 48.6%-66.8% and cost of up to 37.5%, meeting the needs of sustainable development. But the mechanical properties are quite different; the decrease in compressive and flexural strength restricts its use in load-bearing structures. Among the schemes, Scheme 2 had the highest comprehensive performance of 78 points (higher than the 72 points of ordinary cement), with a compressive strength of 15.6 MPa, meeting the requirements for use in non-load-bearing walls and thermal insulation materials. This reveals the performance characteristic of biomass building materials "trading strength for environmental protection," providing a scientific basis for their rational application in low-stress building components.

V. CONCLUSION

Building materials are required to provide sound and sustainable performance for urban noise reduction. Existing sound-absorbing materials face functional and environmental challenges. Combining the reinforcement effect of regenerated cellulose fiber and physical foaming, a cement-based sound-absorbing material system with a gradient pore

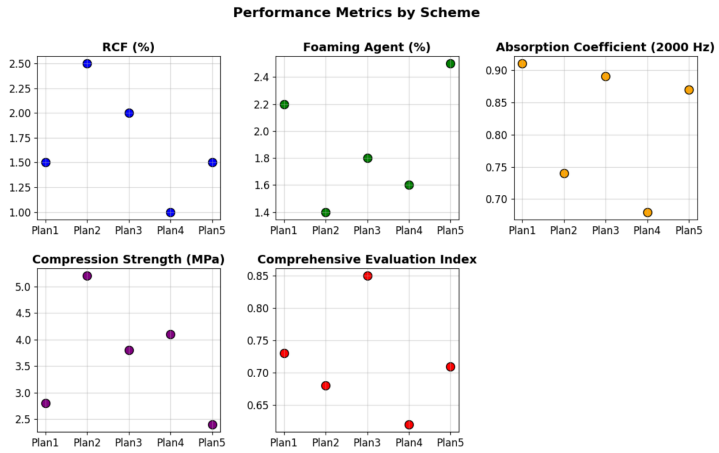

FIGURE 2. Results of Synergistic Optimization of Sound Absorption and Mechanical Properties

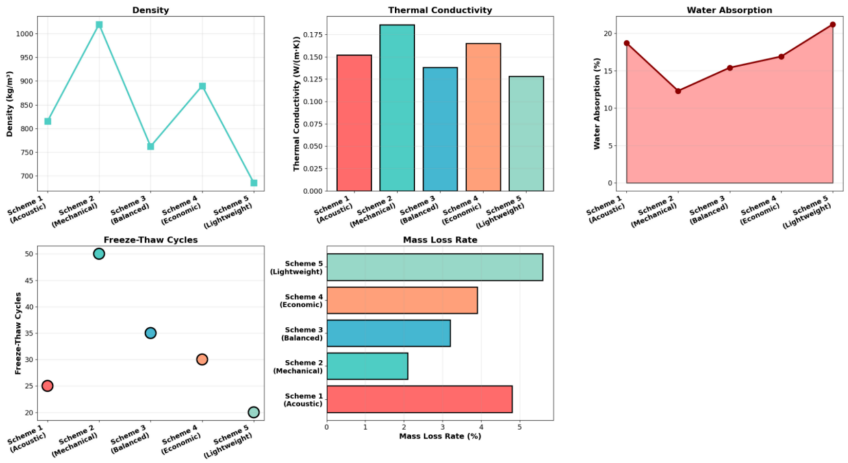

FIGURE 3. Results of Optimization of Thermal and Durability Properties

structure was developed, thus demonstrating the prospect of using waste fibers in sound-absorbing materials. Fiber modification improved the adhesion and crack-propagation of the interface, increasing the material's toughness. Structural design of the porous structure obtained optimal matching of mid-to-high frequency sound energy. This material not only meets the strength requirements for non-loadbearing walls, but also significantly lowers carbon emissions, and provides an opportunity for construction waste recycling. In this paper, the exact control of pore size distribution is not yet fully understood, improvements in low-frequency sound absorption need to be further explored, and the acoustic stability and durability under long-term environmental conditions need to be tested. In the future, multi-scale numerical simulations should be combined to further explore the interaction between pores and sound waves, design composite pore structures to achieve more effective sound absorption in a wider frequency range, and demonstrate on-site applications to assess their noise reduction performance, to promote the integration of materials from the laboratory to the application site, offering comprehensive solutions for improving the acoustic environment of green buildings.

AUTHOR CONTRIBUTIONS

Jipeng Liu designed, collected and analyzed the data, and drafted the manuscript. Jipeng Liu conducted the study, critically revised the manuscript for important intellectual content, and gave final approval of the version to be published. Jipeng Liu participated fully in the work, take public responsibility for appropriate portions of the content, and agreed to be accountable for all aspects of the work in ensuring that questions related to the accuracy or integrity of any part of the work are appropriately investigated and resolved.

CONFLICTS OF INTEREST

The author declares no conflict of interest.

FUNDING

This work was supported by the Project Selected via Open Bidding, Science and Technology Program of Henan Provin-

cial Department of Housing and Urban-Rural Development (Grant No. HNJS-2025-B4).

ACKNOWLEDGEMENTS

Not applicable.

REFERENCES

[1] P. Song, Q. Wang, X. Zhang, and Y. Wang, "Preparation of hemp stalk-based porous carbon and its performance study on polyester needle-punched felt sound-absorbing composite material," Plastics Science and Technology, vol. 54, no. 2, pp. 39-44, 2026, [Online]. Available: http://qikan.cqvip.com/Qikan/Article/Detail?id=7203146835&from=Qikan_Search_Index.

[2] R. Wang, Z. Zhou, X. Feng, Y. Shen, F. Liu, and J. Xing, "Preparation and properties of porous sound-absorbing materials made of polyester fiber and polyethylene/polypropylene bicomponent fiber," Journal of Textile Research, vol. 46, no. 2, pp. 61-68, 2025, [Online]. Available: http://qikan.cqvip.com/Qikan/Article/Detail?id=7200322527&from=Qikan_Search_Index.

[3] J. Xing, F. Liu, M. Yin, and D. Wang, "Innovative comprehensive experimental design for the preparation and performance analysis of fiber-based porous sound-absorbing materials," Polymer Bulletin, vol. 38, no. 8, pp. 1323-1334, 2025, [Online]. Available: http://qikan.cqvip.com/Qikan/Article/Detail?id=7201625622&from=Qikan_Search_Index.

[4] F. Li, B. Xu, H. Chen, M. Zhao, and S. Ge, "New sound-absorbing material and its properties prepared by carbonized cork oak bark fiber combined with silica sol," Adhesion, vol. 53, no. 3, pp. 684-687, 2026, [Online]. Available: http://qikan.cqvip.com/Qikan/Article/Detail?id=7203027272&from=Qikan_Search_Index.

[5] J. Zheng, Y. Xiong, and X. Yin, "Study on pore structure and properties of magnesium phosphate cement-based porous sound-absorbing materials," New Building Materials, vol. 52, no. 4, pp. 61-64+69, 2025, [Online]. Available: http://qikan.cqvip.com/Qikan/Article/Detail?id=7200775017&from=Qikan_Search_Index.

[6] C. Arenas, D. Ríos J, H. Cifuentes, et al., "Sound absorbing porous concretes composed of different solid wastes," European Journal of Environmental and Civil Engineering, vol. 26, no. 9, pp. 3805-3817, 2022, doi: 10.1080/19648189.2020.1824817.

[7] Z. Feng and Y. Liu, "The latest research status of porous sound-absorbing materials," Journal of Polymer Engineering, vol. 45, no. 3, pp. 207-225, 2025, doi: 10.1515/polyeng-2024-0211.

[8] J. Lou, C. He, A. Shui, et al., "Enhanced sound absorption performance of porous ceramics with closed-pore structure," Ceramics International, vol. 49, no. 23, pp. 38103-38114, 2023, doi: 10.1016/j.ceramint.2023.09.140.

[9] N. Rastegar, A. Ershad-Langroudi, H. Parsimehr, et al., "Sound-absorbing porous materials: a review on polyurethane-based foams," Iranian Polymer Journal, vol. 31, no. 1, pp. 83-105, 2022, doi: 10.1007/s13726-021-01006-8.

[10] M. Liang, H. Wu, J. Liu, et al., "Improved sound absorption performance of synthetic fiber materials for industrial noise reduction: A review," Journal of Porous Materials, vol. 29, no. 3, pp. 869-892, 2022, doi: 10.1007/s10934-022-01219-z.

[11] K. Matsuo, K. Imamoto, Y. Li, et al., "Fundamental Experiments on Evaluating the Sound Absorption Coefficient of Porous Concrete," Journal of Asian Concrete Federation, vol. 12, no. 1, pp. 59-65, 2026, doi: 10.18702/acf.2026.12.1.59.

[12] A. Wongkvanklom, P. Posi, P. Kasemsiri, et al., "Strength, thermal conductivity and sound absorption of cellular lightweight high calcium fly ash geopolymer concrete," Engineering and Applied Science Research, vol. 48, no. 4, pp. 487-496, 2021, [Online]. Available: https://ph01.tci-thaijo.org/index.php/easr/article/view/243363.

[13] B. Peceño, M. Perez-Soriano E, D. Ríos J, et al., "Morphological analysis of porosity and sound absorption in sustainable materials from rice husk," Building Acoustics, vol. 29, no. 3, pp. 387-399, 2022, doi: 10.1177/1351010X221103674.

[14] A. Rino, I. Prasetiyo, R. Adhika D, et al., "Development of porous composite ceramic with sugarcane fiber filler for sound absorber materials," Building Acoustics, vol. 31, no. 1, pp. 3-13, 2024, doi: 10.1177/1351010X231209609.

[15] M.M. Abbas, "Recycling waste materials in construction: mechanical properties and predictive modeling of Waste-Derived cement substitutes," Waste Management Bulletin, vol. 3, no. 1, pp. 168-192, 2025, doi: 10.1016/j.wmb.2025.01.004.

[16] S. Thill, T. Schmidt, D. Wöll, et al., "A regenerated fiber from rennet-treated casein micelles," Colloid and Polymer Science, vol. 299, no. 5, pp. 909-914, 2021, doi: 10.1007/s00396-020-04802-5.

[17] Q. Bian, C. Bauer, A. Stadler, et al., "In-situ high temperature and large strain monitoring during a copper casting process based on regenerated fiber Bragg grating sensors," Journal of Lightwave Technology, vol. 39, no. 20, pp. 6660-6669, 2021, [Online]. Available: https://opg.optica.org/jlt/abstract.cfm?uri=jlt-39-20-6660.

[18] Y. Wang, J. Tao, W. Yuan, et al., "Hollow core Bragg fiber integrated with regenerate fiber Bragg grating for simultaneous high temperature and gas pressure sensing," Journal of Lightwave Technology, vol. 39, no. 17, pp. 5643-5649, 2021, [Online]. Available: https://opg.optica.org/jlt/abstract.cfm?uri=jlt-39-17-5643.

[19] C. Helbrecht, M. Langhans, T. Meckel, et al., "Analyses of the effects of fiber diameter, fiber fibrillation, and fines content on the pore structure and capillary flow using laboratory sheets of regenerated fibers," Nordic Pulp & Paper Research Journal, vol. 38, no. 3, pp. 425-440, 2023, [Online]. Available: https://www.degruyterbrill.com/document/doi/10.1515/npprj-2022-0077/html.

[20] K. Moriam, D. Sawada, K. Nieminen, et al., "Towards regenerated cellulose fibers with high toughness," Cellulose, vol. 28, no. 15, pp. 9547-9566, 2021, doi: 10.1007/s10570-021-04134-9.

[21] H. Liu, W. Fan, Y. Miao, et al., "Closed-loop recycling of colored regenerated cellulose fibers from the dyed cotton textile waste," Cellulose, vol. 30, no. 4, pp. 2597-2610, 2023, doi: 10.1007/s10570-022-05002-w.

[22] W. Qiu and X.Y. Liu, "Recent progress of applying mesoscopic functionalization engineering principles to spin advanced regenerated silk fibroin fibers," Advanced Fiber Materials, vol. 4, no. 3, pp. 390-403, 2022, doi: 10.1007/s42765-021-00127-2.

[23] J. Li, S. Lu, F. Liu, et al., "Structure and properties of regenerated cellulose fibers based on dissolution of cellulose in a CO2 switchable solvent," ACS Sustainable Chemistry & Engineering, vol. 9, no. 13, pp. 4744-4754, 2021, doi: 10.1021/acssuschemeng.0c08907.

[24] Q. Li, Z. Yuan, C. Zhang, et al., "Tough, highly oriented, super thermal insulating regenerated all-cellulose sponge-aerogel fibers integrating a graded aligned nanostructure," Nano Letters, vol. 22, no. 9, pp. 3516-3524, 2022, doi: 10.1021/acs.nanolett.1c03943.